



RESEARCH ARTICLE SUMMARY

SEISMOLOGY

Fault size–dependent fracture energy explains multiscale seismicity and cascading earthquakes

Alice-Agnes Gabriel*, Dmitry I. Garagash, Kadek H. Palgunadi, P. Martin Mai

INTRODUCTION: The catastrophic consequences of large earthquakes governed by complex, multifault rupture dynamics, such as the 6 February 2023 Kahramanmaraş, Türkiye, earthquake doublet. The intricate mechanics of earthquakes, however, remain poorly understood. Natural fault zones are structurally complex systems, comprise fractures and faults of millimeters to hundreds of kilometers in length, and may generate earthquakes over many orders of magnitude. But the details of the earthquake energy budget, its scaling properties, and how multiscale fractures and faults interact dynamically remain enigmatic.

RATIONALE: Traditionally, estimates of fracture energy, the average energy dissipated during

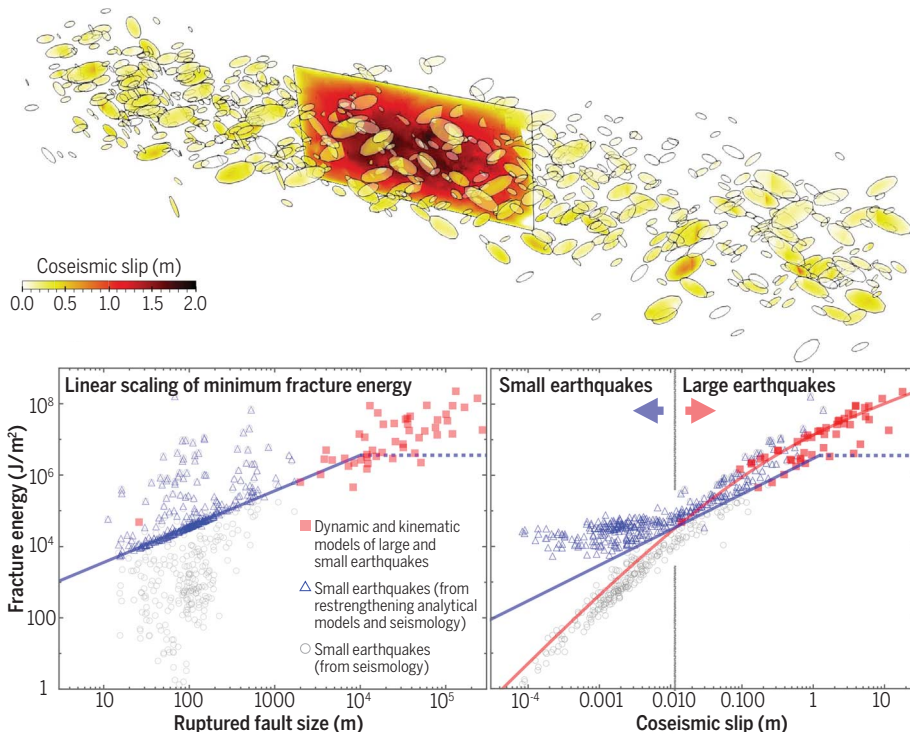
an earthquake, are derived from seismological observations by using idealized earthquake models. Utilizing advanced mechanical models of earthquake rupture propagation, we introduced physics-based corrections for seismologically observed fracture energy and developed analytical descriptions of three-dimensional (3D) cracklike circular dynamic ruptures with flash-heating friction and coseismic restrengthening as well as bilaterally expanding kinematic pulse-like ruptures with coseismic stress recovery. We synthesized global seismological observations earthquakes with physics-based corrections to estimate the total earthquake fracture energy across a range of rupture sizes. We added fracture energy computed from 12 3D rupture simulations of past small repeating

and large earthquakes spanning magnitude of 1.9 to 9.2. We found that the dynamic weakening and typically neglected restrengthening effects are important for the energy budget of small earthquakes.

RESULTS: Our analysis reveals a linear scaling relationship between a minimum fracture energy and ruptured fault size that is independent of rupture propagation details. We propose that fundamentally different fracture processes govern small and large earthquakes. This explains the linear scaling of the minimum “small-slip” fracture energy with ruptured fault size and implies a fundamental break in earthquake scaling with slip. The minimum fracture energy reflects a local fault property, which can be explained by a well-localized near-front process zone. By contrast, a possibly fault-invariant part of fracture energy increases continuously with earthquake slip and dominates at large slip.

We used supercomputing simulations to demonstrate how fault size–dependent fracture energy facilitates the complex mechanisms driving cascading earthquake nucleation, propagation, and arrest with implications for multifault and multiscale earthquake sequences. We simulated 3D dynamic earthquake rupture and interaction across more than 700 partially intersecting fractures in the damage zone of a planar strike-slip fault. We unveiled large dynamic rupture earthquake cascades involving multiscale fractures within the fault damage zone, which can host ruptures spanning four orders of moment magnitude. These models represent a paradigm shift beyond typical physics-based earthquake models, which often idealize fault zones as infinitesimally thin interfaces with separated on- versus off-fault rheologies. The resulting dynamic rupture cascades can generate large earthquakes consisting only of distributed, multiscale slip across the fault zone fractures. These cascades may or may not dynamically trigger main-fault rupture.

CONCLUSION: We offer a simple explanation for seismicity across scales and provide insight into earthquake genesis and multifault rupture cascades. Our proposed scaling of fracture energy aligns with cascading earthquake observations and the physical mechanisms of localization of brittle deformation before and during earthquakes, implying a fundamental change in the mechanics of earthquake rupture with slip. ■



A simple explanation for earthquakes observed across all scales with implications for earthquake nucleation and multifault rupture cascades. (Top) Supercomputing simulation of a 3D multiscale and multifault earthquake cascade across >700 fractures in a fault damage zone redistributing stresses that may assist or inhibit dynamic triggering of a larger earthquake on the main fault. Earthquake slip is shown on the fractures and main fault in an “exploded” side view. (Bottom left) Linear scaling between the “small-slip” minimum earthquake fracture energy and ruptured fault size. (Bottom right) Break in scaling of total fracture energy with slip between the “small-slip” fault property and the continuously increasing “large-slip” component, implying a fundamental change in the mechanics of earthquake rupture with slip.

The list of author affiliations is available in the full article online.
*Corresponding author. Email: algabriel@ucsd.edu
Cite this article as A.-A. Gabriel *et al.*, *Science* **385**, ead9587 (2024). DOI: [10.1126/science.ad9587](https://doi.org/10.1126/science.ad9587)

READ THE FULL ARTICLE AT
<https://doi.org/10.1126/science.ad9587>

RESEARCH ARTICLE

SEISMOLOGY

Fault size–dependent fracture energy explains multiscale seismicity and cascading earthquakes

Alice-Agnes Gabriel^{1,2*}, Dmitry I. Garagash³, Kadek H. Palgunadi^{4,5,†}, P. Martin Mai⁴

Earthquakes vary in size over many orders of magnitude, often rupturing in complex multifault and multievent sequences. Despite the large number of observed earthquakes, the scaling of the earthquake energy budget remains enigmatic. We propose that fundamentally different fracture processes govern small and large earthquakes. We combined seismological observations with physics-based earthquake models, finding that both dynamic weakening and restrengthening effects are non-negligible in the energy budget of small earthquakes. We established a linear scaling relationship between fracture energy and fault size and a break in scaling with slip. We applied this scaling using supercomputing and unveiled large dynamic rupture earthquake cascades involving >700 multiscale fractures within a fault damage zone. We provide a simple explanation for seismicity across all scales with implications for comprehending earthquake genesis and multifault rupture cascades.

Seismic hazard assessments are necessary because individual earthquakes cannot be predicted or prevented. As demonstrated by the multifault 2023 Kahramanmaraş earthquake doublet in Türkiye (1, 2), our poor understanding of complex earthquake dynamics has potentially catastrophic consequences. Well-recorded large earthquakes and small labquakes alike reveal a striking variability of earthquake dynamics, often including cascading multifault and multievent earthquake sequences across complicated fault geometries. Despite the growing body of diverse earthquake observations (3), fundamental questions remain unanswered, including that of the governing driving factors of cascading dynamic rupture and the interaction and apparent self-similarity of small and large earthquakes (4–6).

Earthquakes result from catastrophic failure of brittle rocks under tectonic stresses, involving highly nonlinear processes across fault structures embedded in three-dimensional (3D) geology. Natural fault zones are multiscale systems spanning millimeters to thousands of kilometers in fracture and fault lengths (7–10). Owing to their structural complexity, natural faults and fractures may generate earthquakes spanning many orders of magnitude ($-4 < M < 9$, with M being an earthquake magnitude

(11–13). Traditionally, earthquake frictional shear failure has been analyzed through the lens of fracture mechanics (14, 15), governed by scale-independent material parameters. However, a paradigm shift supported by laboratory and field studies (16, 17) suggests a scale-dependent nature of fracture energy challenging long-standing beliefs. Subsequently, various scaling relations between fracture energy and earthquake source characteristics have been proposed (11, 18–23).

Yet, constraining the scaling of earthquake rupture properties from observations remains inherently challenging (12). A paucity of observations, which are sparse in both time and space, limits our ability to measure small-scale processes and to understand the underlying physics of earthquakes (24). Additionally, the dynamics of fault slip is a problem mostly unsolvable analytically.

Simple empirical scaling relations connect small and large faults and earthquakes occurring on them with models of elliptical cracks and linear-elastic fracture mechanics (25). Empirical fault constitutive relations, i.e., friction laws (7) informed by small-scale laboratory experiments, are useful to describe coseismic fault weakening that controls earthquake nucleation, dynamic slip evolution, and rupture arrest. Their parameterization, however, differs by up to several orders of magnitude when inferred from laboratory experiments versus observations from real earthquakes (11, 26). This has either been explained by a scale dependence of the structural complexity or by coseismic frictional weakening processes (16) of faults.

In this study, we integrate analytical and numerical models with seismological data, offering a unified perspective on the scaling of earthquake dynamics. We propose that fun-

damentally different “small-slip” and “large-slip” fracture processes govern the physics of small versus large earthquakes and how they interact dynamically, as well as a break in scaling with slip. We show that fault size-dependent fracture energy is crucial in facilitating the activation of multifault ruptures within a multiscale fault network. Our models introduce a degree of realism beyond typical physics-based earthquake models, which often idealize fault zones as infinitesimally thin interfaces with distinct on- versus off-fault rheologies. Our proposed mechanism resembles a dynamic cascading earthquake nucleation model (27) and aligns with the physical mechanism of localization of brittle deformation before and during earthquakes.

The earthquake energy budget

The energy budget of earthquake rupture (Fig. 1) describes the dissipation of the released energy during the dynamic evolution of fault stress with slip and the radiation of seismic waves (28). Its components are, however, difficult to disentangle and quantify from observations. Specifically, their potential scale dependence or fault-invariant character remains debated (11, 18). During earthquake rupture, the total strain energy release per unit of the ruptured surface at a given point of the fault is given by $\Delta W = (\tau_0 + \tau_1)\delta/2$, whereby τ_0 and τ_1 are the initial and final shear stresses, respectively, and δ is the final coseismic fault slip.

The (local) total strain energy release ΔW can be divided into several components forming the earthquake energy budget (Fig. 1A) (29, 30): \mathcal{E}_s , the energy radiated by seismic waves (31); G , the fracture energy; W_r , the restrengthening work (32); and F , the frictional heat. This local energy budget can be averaged over the entire fault rupture area (33). The exact partitioning between frictional heat ($F = \tau_d\delta$) and total mechanical work (breakdown work and restrengthening work, $G + W_r$) is still a matter of debate (11). We adopt the common assumption that it is marked by the minimum dynamic fault strength τ_d .

Fracture energy G balances the release of ΔW with several dissipative mechanisms (Fig. 1A). If the rate at which the stored elastic strain energy ΔW of the prestressed host rock is released at the rupture front and exceeds the fracture energy G , then faults or fractures of any size may generate earthquakes. G represents the entire breakdown work required to reduce fault strength from its peak value, τ_p , at the onset of slip, to a minimum dynamic strength, τ_d , over a critical slip distance, δ_c (Fig. 1A), omitting the initial displacement hardening effect (34, 35). The fracture energy per unit area can be defined as $G = \int_0^{\delta_c} [\tau(s) - \tau_d] ds$, with s being a slip integration variable (29). Its average over the ruptured fault area can be expressed from the earthquake energy budget as:

¹Scripps Institution of Oceanography, University of California San Diego, La Jolla, CA, USA. ²Department of Earth and Environmental Sciences, Ludwig-Maximilians-Universität München, Munich, Germany. ³Department of Civil and Resource Engineering, Dalhousie University, Halifax, Canada. ⁴Physical Science and Engineering, King Abdullah University of Science and Technology, Thuwal, Saudi Arabia. ⁵Geophysical Engineering Department, Institut Teknologi Sepuluh Nopember, Surabaya, Indonesia.

*Corresponding author. Email: algabriel@ucsd.edu

†Present address: Swiss Seismological Service, ETH Zürich, Zürich, Switzerland.

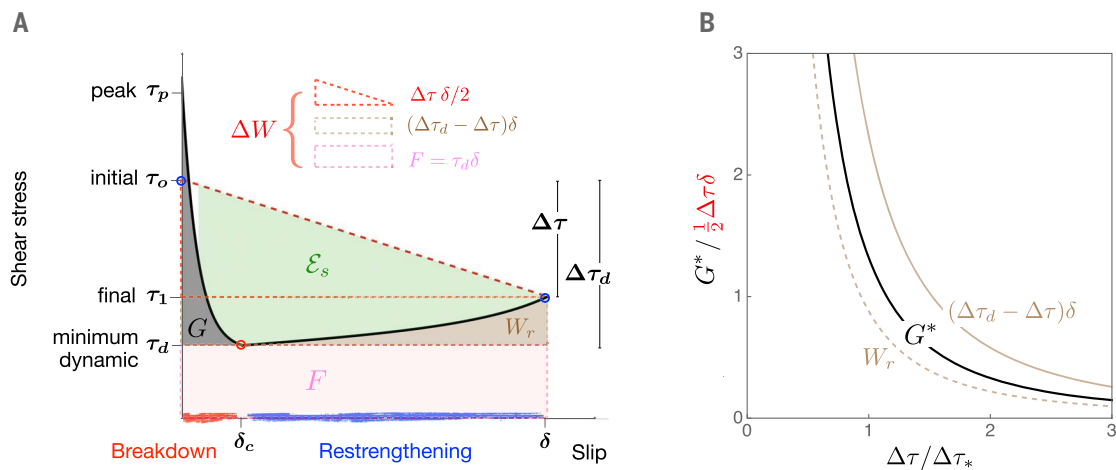


Fig. 1. The earthquake energy budget, including dynamic weakening and restrengthening. (A) Diagram of the total, point-wise earthquake energy budget: \mathcal{E}_s is the energy radiated by seismic waves, W_r is the restrengthening work, F is the frictional heat, and G is the fracture energy often referred to as the breakdown work. We split G into $G' = \frac{1}{2}\Delta\delta - \mathcal{E}_s$ and an often omitted component $G^* = G - G' = (\Delta\tau_d - \Delta\tau)\delta - W_r$. The average of G' over the entire rupture area is seismologically

inferable. G^* results from dynamic over- or undershoot. (B) Normalized $G^* = G - G'$, the difference between the fracture energy G and its seismologically observable portion G' , as a function of the normalized stress drop $\Delta\tau$ from an analytical model of a circular cracklike dynamic rupture with flash-heating friction and coseismic fault restrengthening. The beige curves depict the components of $G^* = (\Delta\tau_d - \Delta\tau)\delta - W_r$, corresponding to the dynamic stress undershoot and restrengthening, respectively.

$$G = \underbrace{\Delta\tau\delta/2 - \mathcal{E}_s}_{G'} + \underbrace{(\Delta\tau_d - \Delta\tau)\delta - W_r}_{G^*} \quad (1)$$

with $\Delta\tau_d = \tau_o - \tau_d$ being the dynamic stress drop; $\Delta\tau$, the static stress drop; G' , the seismologically inferred part of fracture energy, and $G^* = G - G'$.

Although fracture energy fundamentally affects all aspects of the coseismic rupture process, including the nucleation of small and large earthquakes, radiation of potentially destructive seismic waves, and rupture arrest, only a part of G in Eq. 1 (G') is potentially inferable from seismological observations (11, 12, 30). G' is not necessarily representative of the physical quantity of fracture energy because other parts of G , including a multitude of intensely debated coseismic fault weakening and restrengthening processes, remain largely undetectable (32, 36). Using kinematic or dynamic finite-source inversion of large earthquakes allows estimation of the total G (32, 37) but with considerable uncertainties. Dynamic rupture complexity, including self-healing slip pulses (38) and arresting cracks (28), may lead to stress “under- or overshoot” (36), i.e., fault stresses remaining above or below the level expected based on the coseismic slip. Although the effects of dynamically evolving fault stress under- or overshoot are commonly omitted when estimating G (11, 12), we introduce $G^* = G - G'$, which includes stress under- or overshoot and the restrengthening work $W_r = \int_{\delta_c}^{\delta} [\tau(s) - \tau_d] ds$. Therefore, G^* is associated with the dynamic evolution of fault stress during coseismic slip.

The seismologically estimated G' has been inferred to increase with earthquake slip

(11, 12, 39). Several hypotheses have been proposed to explain this key observation and the general variability of G' , including (i) the effect of continuous, possibly fault-invariant, coseismic weakening with slip on all scales, for example, owing to thermal pressurization of pore fluids or flash heating (17, 22, 40) and (ii) fault properties, such as fault size, fault maturity, fault rheology, and frictional parameters, or prestress heterogeneity (7, 18) that determine fracture energy scaling. Numerical solutions for cracklike earthquake sources without dynamic restrengthening (36) show only small dynamic overshoot, which often serves as justification for assuming that $G \approx G'$ when inferring the fracture energy of small and large earthquakes (12, 20, 29). However, G has been estimated to be an order of magnitude larger than G' (22), and non-negligible G^* is a common characteristic of more realistic physics-based earthquake models (41, 42), which may substantially affect fracture energy estimates (30).

Physics-based correction of observed fracture energy

We developed physics-based corrections G^* for the observationally inferred fracture energy G' from advanced analytical models of the mechanics of earthquake rupture propagation. Accurately estimating fracture energy G is crucial for understanding the physics of earthquakes. However, the seismologically estimated G' only approximates G under the common assumption that the effects of dynamic restrengthening and fault stress under- or overshoot (G^*) are negligible. We found that G^* linearly correlates with rupture size R , regardless of

rupture propagation specifics. G^* becomes particularly important for earthquakes characterized by small stress drops.

To reconcile seismological observations with earthquake physics, we first explicitly quantified G^* using a model of a circular cracklike dynamic rupture with flash-heating friction (fig. S1) and coseismic fault restrengthening (figs. S2 and S3). We then confirmed the non-negligible contribution of coseismic restrengthening and stress under- or overshoot (36) to the fracture energy of earthquakes with a model of a bilaterally expanding kinematic pulse-like rupture with coseismic stress recovery in the wake of the pulse.

Analytical models

Earthquake rupture, whether cracklike or pulse-like, driven by rate-dependent friction (41, 43) or thermal pressurization (41, 44–46), leads to fault stress recovery. This contributes to dynamic stress undershoot during earthquake rupture and challenges the assumption that G^* is negligible, thereby adversely affecting the accuracy of estimating G . Deriving an analytical description of a circular cracklike dynamic rupture of size R , driven by rapid flash-heating frictional weakening at high slip velocity (fig. S1) (41, 47, 48), we approximated dynamic earthquake rupture as a self-similar singular Kostrov solution (28) and account for time-varying rupture speed and stress drop. At high slip velocity ($V \gg V_w$, with V_w being the critical weakening slip velocity) and for sufficiently large coseismic slip ($\delta \gg L$, with L being the state evolution slip distance), we defined two separate scales to characterize cracklike dynamic rupture (14, 49, 50):

(i) The tip of the rupture: The near-front process zone experiences strength degradation from a peak value, τ_p , precipitated by the direct friction effect ahead of the advancing rupture front. The dynamic fault strength then transitions to a fully weakened steady state, $\tau_{ss} = \tau_w$, during slip comparable to L . These near-tip processes can be approximated by a rupture front speed (v_r)-dependent crack-tip singularity defined by the fracture energy of the breakdown process in the near-front process zone, $G_c(v_r) \approx [\tau_p(v_r) - \tau_w]L$.

(ii) The body (or tail) of the rupture: Away from the rupture front, the fault strength remains approximately at steady state, $\tau_{ss}(V)$, and thus recovers as the slip rate $V(r, t)$ decreases with distance from the rupture front.

We build on the approach of (50), which was developed to study cracklike 1D rupture on a fault with classical (non-flash-heating) rate- and state-dependent friction. We outline our adaptation to 3D circular cracks driven by flash-heating in (51). Figure S2 illustrates how this model describes the spatial distribution of the normalized coseismic restrengthening.

By analyzing the stress distribution and slip history during rupture, we derived analytical expressions for G^* and its components (Fig. 1B and fig. S3) (51). We found that we can express the average G^* solely in terms of rupture size R , as

$$G^* = 0.4393 \times \tau_* R \quad (2)$$

with

$$\tau_* = (\tau_{LV} - \tau_w) \frac{V_w}{v_r},$$

where the dynamic stress prefactor τ_* is calculated from the flash-heating breakdown strength ($\tau_{LV} - \tau_w$). Here, τ_{LV} is the low-velocity steady-state dynamic stress (fig. S1). The factor 0.4393 is exact and emerges from the analytically modeled stress and slip distributions of a circular crack driven by flash-heating frictional weakening at the dynamic rupture front and accounting for restrengthening in its body. In this analytic framework, our derivation does not rely on a single fixed set of frictional stress properties. In Eq. 2, only the prefactor τ_* is affected by how we parameterize the analytical model. Although rupture size R varies over many orders of magnitude, the changes in the dynamic stress prefactor τ_* due to different model parameters are minor in comparison.

The linear scaling of G^* with R is not specific to our analytical model of a flash-heating cracklike dynamic rupture. We derived a comparable quasilinear scaling of G^* with R for a kinematic pulselike analytical model (51). This generalization is particularly notable, given the fundamentally different spatiotemporal modes of rupture development assumed in the respective models. During cracklike rupture, the fault slips continuously over the entire ruptured area, and the slip continues through-

out the rupture duration until arrest fronts arrive from the terminal edges of the rupture (52). By contrast, in a pulselike rupture (53), frictional strength weakens only transiently, and the rupture front is closely followed by a healing front, which leads to slip occurring only over a small portion of the fault at any given point in time during rupture propagation (38).

In the pulselike model, our proposal that dynamic undershoot scales linearly with rupture size, a central aspect of our proposed scaling of G^* , is based on how stress recovers in the wake of a pulselike rupture. In our cracklike model, an analytical description of friction is necessary to describe how stress recovers behind the tip (figs. S2 and S3). By contrast, in the wake of a pulselike rupture in which the slip has stopped and the fault is relocked, we rely only on elasticity to describe stress recovery, irrespective of the specific physical processes driving the pulse.

Both analytic models are necessarily simplified representations of earthquake rupture. For example, they assume a constant prestress, in contrast to the heterogeneous prestress state that will govern the 3D dynamic rupture fracture network simulations in the section titled “Multifault earthquake cascades in 3D dynamic rupture simulations with fault size-dependent fracture energy.”

Stress-drop dependence

By considering the dynamic contributions of coseismic restrengthening and stress under- or overshoot effects, we show that in contrast to common assumptions, G^* does play a substantial role in the earthquake energy budget. In Eq. 2, which expresses G^* in terms of source size R , G^* is independent of the average coseismic stress drop $\overline{\Delta\tau}$. G^* is also independent of rupture propagation details, as demonstrated in an alternative expression (51) of G^* in terms of average stress drop $\overline{\Delta\tau}$ and average slip $\langle\delta\rangle$ across the rupture radius R :

$$G^* = 0.6589 \times \frac{\Delta\tau^2}{\overline{\Delta\tau}} \langle\delta\rangle. \quad (3)$$

Quantitatively comparing G^* to the positive portion of G' , which is the average of $\frac{1}{2}\Delta\tau\delta$ (Eq. 1), we see that G^* is negligible for large-stress drop events but becomes important and even dominant for earthquakes with stress drops comparable to or smaller than the restrengthening scale $\Delta\tau_* \sim \sqrt{\mu\tau_*}$ (Fig. 1B). We fixed neither the stress drop nor the undershoot in our analysis, allowing us to infer that G^* constitutes a significant portion of G if the stress drop is smaller than or similar to the restrengthening scale $\Delta\tau_*$. We estimate that $\tau_* \approx 800$ Pa and that the critical $\Delta\tau_* \approx 5$ MPa for a plausible model parametrization (51).

Linearly scale-dependent fracture energy

We derived a simple linear scaling relationship between fracture energy and fault size

and a break in scaling with slip (Fig. 2). We utilized the physics-based estimate of G^* (Eq. 2) to determine the total fracture energy $G = G' + G^*$, corrected for coseismic rapid dynamic weakening and restrengthening, from seismologically inferred G' observations of small earthquakes (22). Unlike for G' , no correction was applied to total fracture energy G estimates of large earthquakes (22, 32). We added measures of G from 12 data-constrained realistic 3D rupture simulations of past small and large well-recorded earthquakes spanning moment magnitudes (M_w) of 1.9 to 9.2 (table S1) (51). These included the 2023 M_w 7.8 and 7.7 Kahramanmaraş, Türkiye, and the 2019 M_w 6.4 and 7.1 Ridgecrest, California, earthquake sequences (1, 54); the 2017 M_w 5.5 Pohang, South Korea, induced earthquake (55); the 2016 M_w 6.2 Amatrice, Italy, normal faulting (56); the 2019 M_w 7.5 Palu, Sulawesi, supershear (57); the 1992 M_w 7.1 Landers, California, multisegment (58); the 2016 M_w 7.8 Kaikoura, New Zealand, mixed faulting (59); and the large 2004 M_w 9.2 Sumatra megathrust (60) earthquakes, as well as models of smaller repeating earthquakes, such as the M_w 1.9 San Andreas Fault repeating sequence in Parkfield, California, (61) and the M_w 4.8 Kamaishi, Japan, (62, 63) repeating sequence.

We found an evident steady increase in fracture energy with ruptured fault size (Fig. 2A), consistent with the scaling of G^* that we established, but not with fault slip (Fig. 2B). This scaling contradicts previous inferences of fracture energy G rising with both earthquake slip and earthquake size across all scales, such as in the uncorrected inferences of G' (gray symbols, Fig. 2).

To explain this scaling behavior, we proposed that the total fracture energy G comprises two independent and equally important components: (i) $G_c(R)$, a “small-slip” minimum fracture energy that is a fault property linked to the ruptured fault size R and that dominates faulting at small-slip scales, and (ii) $\Delta G(\delta)$, a “large-slip” and possibly fault-invariant part of fracture energy that increases continuously with coseismic slip δ , as

$$G = G_c(R) + \Delta G(\delta). \quad (4)$$

Thermal pressurization leads to continuous weakening on all slip scales (20). The effect of such enhanced, continuing weakening is included in this decomposition of fracture energy as $\Delta G(\delta)$. However, the corrected fracture energy exceeds the prediction of a continued slip-weakening model (22), $G > \Delta G(\delta)$. For smaller earthquakes, our proposed correction $G^*(R)$ dominates the seismological G' estimates. There are exceptions, particularly for earthquakes with larger estimated G' , such as the Friuli, Italy, sequence, where total fracture energy G and G' are more comparable (blue open triangles, Fig. 2A).

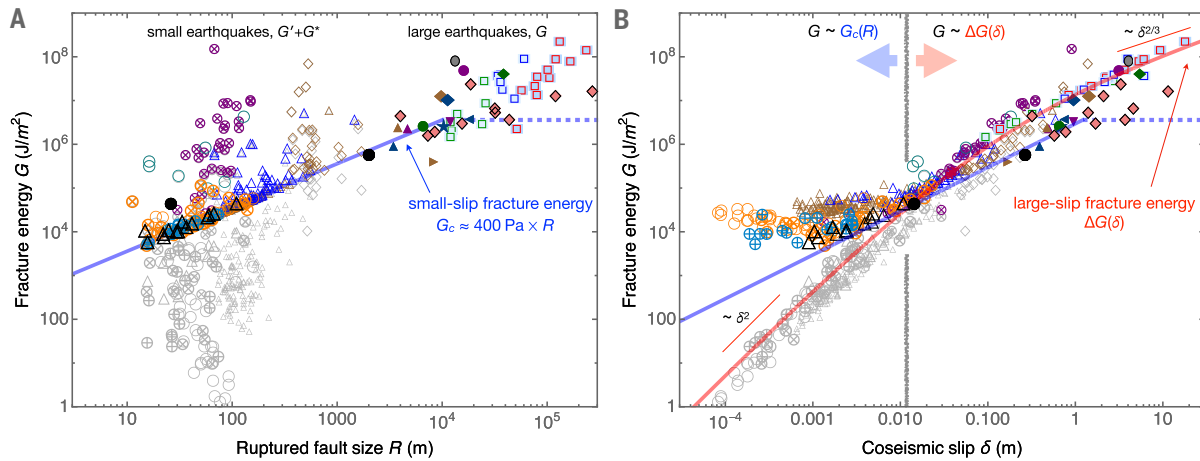


Fig. 2. Linearly scale-dependent fracture energy composed of a “small-slip” fault property and a continuously increasing “large-slip” component. (A) Fracture energy G versus ruptured fault size R for small and large crustal earthquakes and subduction zone earthquakes (colored symbols) (fig. S4). Small crustal earthquakes (colored open symbols) include our physics-based correction G^* of the observationally inferred G' (gray open symbols) (22). For larger crustal and subduction zone earthquakes, fracture energy G can be estimated directly, and we show (total) G (32) and G_{\max} (22) as colored filled symbols. The pink-filled diamonds and black circles are (total) G calculated from data-constrained 3D earthquake simulations of past well-recorded

earthquakes spanning M_w 1.9 to 9.2 (table S1). The blue line marks the minimum fracture energy $G_c(R) = 359.5205 \text{ Pa} \times R \approx 400 \text{ Pa} \times R$, which we term “small-slip” fracture energy. (B) The same as (A) but G plotted versus coseismic slip δ . The blue line represents the constant stress-drop scaling of the small-slip fracture energy with slip, $G_c \approx 3.3 \text{ MPa} \times \delta$, assuming $\Delta\tau = 5 \text{ MPa}$ (51). The red line shows the theoretically predicted fracture energy increase due to thermal pressurization with coseismic slip (22), which we call “large-slip” fracture energy. The gray line marks the break in scale at a cross-over slip of $\approx 0.01 \text{ m}$, where both the small-slip and large-slip contributions to fracture energy are comparable. See also figs. S4 and S5.

Challenging the common assumption that $G \approx G'$ allowed us to accurately estimate a scaling of the minimum G , G_c , with ruptured fault size R . We propose that $G_c(R)$ is a local fault property, which can be explained by a well-localized near-front process zone and depends on fault size [supplementary materials section “Scaling of state evolution slip distance with fault size” (51)]. This minimum fracture energy $G_c(R)$ emerges as a simple linear function of ruptured fault size (Fig. 2A), with

$$G_c(R) \approx 400 \text{ Pa} \times R. \quad (5)$$

Earthquakes with fracture energy above this lower bound may have experienced additional weakening or represent partial ruptures. We assumed in our analysis that the observed ruptured fault size R is representative of the full fault size, i.e., that a representative subset of the data corresponds to earthquakes that have ruptured nearly the entire area of their corresponding faults.

We found a clear break in the scaling of the total fracture energy G with coseismic slip δ (Fig. 2B) at a cross-over slip of $\delta \approx 0.01 \text{ m}$. For large earthquakes, continuous weakening described by the large-slip fracture energy, $G \approx \Delta G(\delta)$, becomes dominant over the small-slip fault property $G_c(R)$. This break in scaling is not an artifact of specific datasets or specific seismological techniques (fig. S4). This result quantifies a testable threshold in coseismic slip beyond which the mechanics of earthquake rupture fundamentally change, which signifies a tangible and measurable shift in

the fracture energy and mechanical behavior of faults.

Our findings reflect fracture energy as both a fault property and as fault invariant, which are not mutually exclusive but can be reconciled by earthquakes driven by different weakening mechanisms, with distinctive scaling behavior activated at different levels of coseismic slip governed by fracture energy decomposition (Eq. 4). Although we do not anticipate regional and methodological differences in seismological source estimates to bias the observed scaling break (fig. S5), we acknowledge substantial uncertainties in measurements of earthquake source parameters [supplementary materials section “Methods to infer fracture energy for small and large earthquakes” (51)]. We demonstrate the robustness of our scaling (fig. S6) with varying dynamic prefactors in the linear relationship for G^* and show that the value of the cross-over slip, demarcating the transition of small earthquakes dominated by the small-slip fracture energy $G_c(R)$ from large earthquakes dominated by the large-slip fracture energy $\Delta G(\delta)$, varies by a factor of approximately three when τ_* changes by a factor of two.

Multifault earthquake cascades in 3D dynamic rupture simulations with fault size-dependent fracture energy

Including our simple linear scaling of the minimum fracture energy with fault size, $G_c(R)$ (Eq. 5), allowed us to model cascading earthquakes occurring over a multiscale fracture

network and interacting with an embedded main fault (Fig. 3 and fig. S6). Leveraging high-performance computing (at a total cost of ≈ 3.6 million core hours; table S3) enabled us to show that fault size-dependent fracture energy is crucial in facilitating the complex mechanisms driving cascading earthquake nucleation, propagation, and arrest, with implications for multifault earthquake sequences (54). The resulting dynamic rupture cascades are capable of generating large earthquakes, consisting of distributed slip across the fault zone that can dynamically trigger main-fault earthquakes.

Dynamic rupture modeling may involve varying characteristic slip distances across different fault or stress heterogeneity scales (19, 21) to capture rupture growth. We explicitly modeled dynamic earthquake rupture and interaction across 721 multiscale, partially intersecting fractures and an embedded planar strike-slip fault that can host ruptures spanning four orders of moment magnitudes ($M_w = 2$ to 6). In our 3D simulations, earthquake rupture dynamics and the cascading potential to dynamically branch or “jump” multiple fractures and faults are largely controlled by the scale-dependent $G_c(R)$ and by the dynamic stress drop relative to the maximum dynamic strength reduction, the relative prestress ratio \mathcal{R} (fig. S7) (51). We introduce a fracture scale-dependent state evolution slip distance (41), L , directly informed by the scale dependence of the minimum fracture energy $G_c(R)$ (supplementary materials section “Scaling of state evolution slip distance with fault size,” Eq. 31).

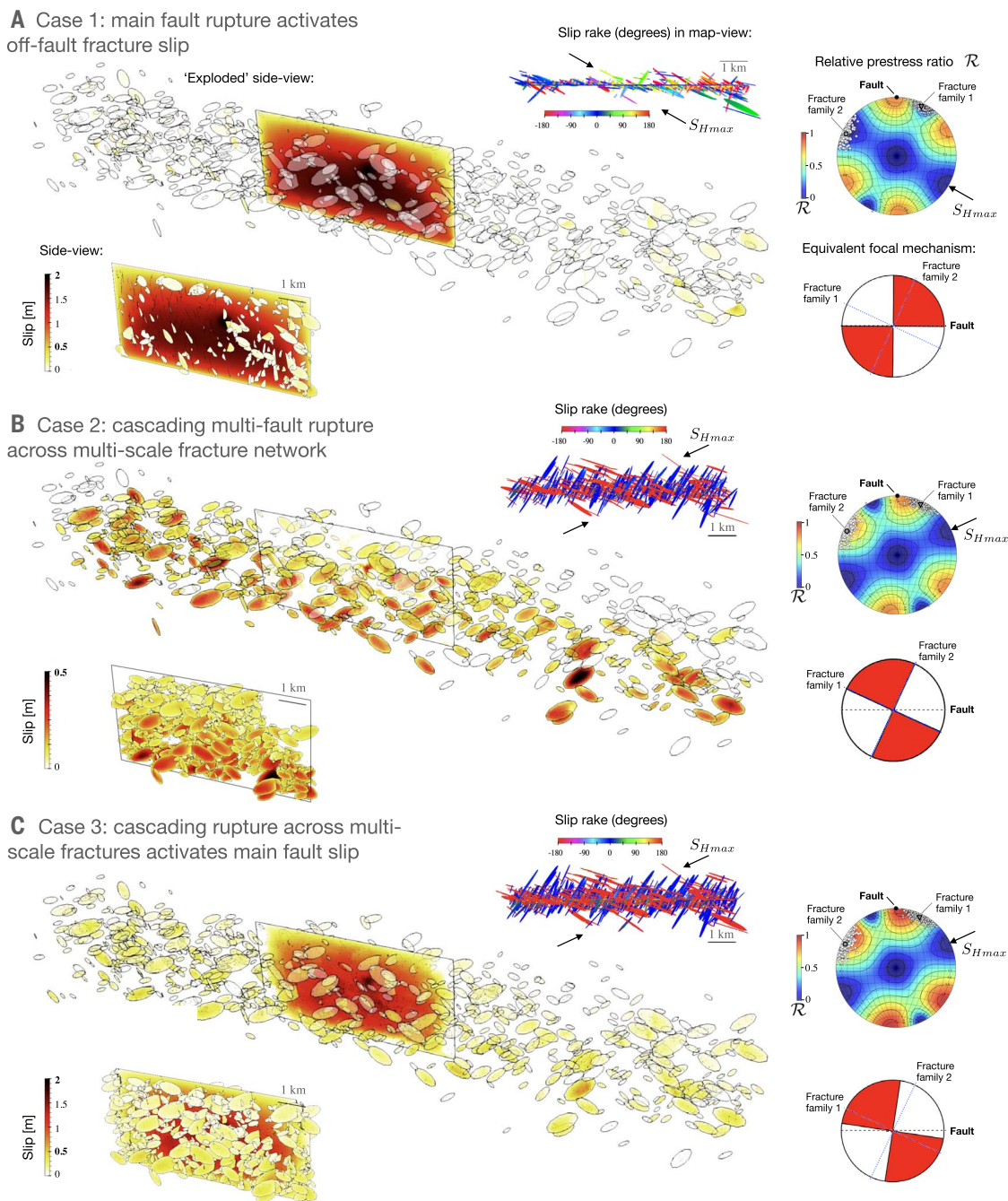


Fig. 3. 3D dynamic rupture simulations. Simulations in a multiscale fracture network with linearly size-dependent fracture energy demonstrate multifault “earthquake cascades” in a fault damage zone interacting with an embedded planar right-lateral strike-slip main fault. We present three simulations with varying ambient prestress conditions. Slip is shown on the fractures and main fault in an “exploded” side view, where interfracture horizontal distances are scaled by a factor of 3.5, and in an unscaled side view. The final slip rake angle of all ruptured fractures of the network or main fault is displayed.

The prestress state is highly heterogeneous (fig. S7) across the different scales of the fracture network: The local prestress conditions for each fracture and the main fault are modulated by their geometry and orientation within the variable ambient stress field. Two fracture

families form an average angle of 100° to each other and angles of 25° and -65° with respect to the main fault’s strike (fig. S6). The orientations of both fracture families vary statistically within $\pm 10^\circ$ in strike and dip, thereby introducing additional prestress heterogeneity. The assumed

Stereoplots show the fault or fracture-local relative prestress ratio (\mathcal{R} , which is the ratio of the maximum possible stress drop and frictional strength drop in a lower hemisphere projection). **(A)** Case 1: Main fault dynamic rupture dynamically activates off-fault fracture network slip ($M_w = 5.96$). See also Movie 1. **(B)** Case 2: Cascading rupture sustained within the fracture network ($M_w = 5.64$). See also Movie 2. **(C)** Case 3: Multifracture dynamic rupture cascade dynamically activating main fault slip after 2.1 s ($M_w = 6.00$). See also Movie 3.

effective normal stress is depth dependent. For a detailed analysis with a different, listric thrust fault geometry, we refer to (64).

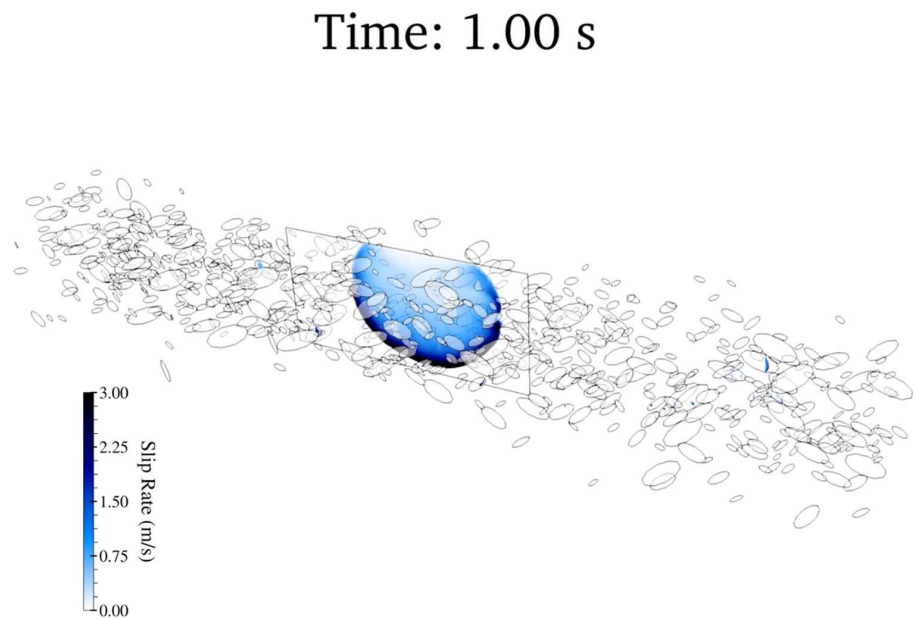
We show three cases (Fig. 3), all initiating dynamic rupture at the same hypocenter but varying in their prestress conditions and orientation

of the maximum ambient horizontal stress (S_{Hmax}) relative to the fractures and the main fault (fig. S7). This results in distinctly different rupture dynamics, and hence, variations in kinematics and overall earthquake slip patterns, but comparable moment magnitudes. Stereoplots (Fig. 3) show more or less optimally oriented fractures and the main fault orientation with respect to the maximum compressive ambient stress S_{Hmax} (fig. S6). The resulting equivalent point-source focal mechanism demonstrates the apparent far-field source mechanisms in comparison to the orientation of both fracture families and the main fault.

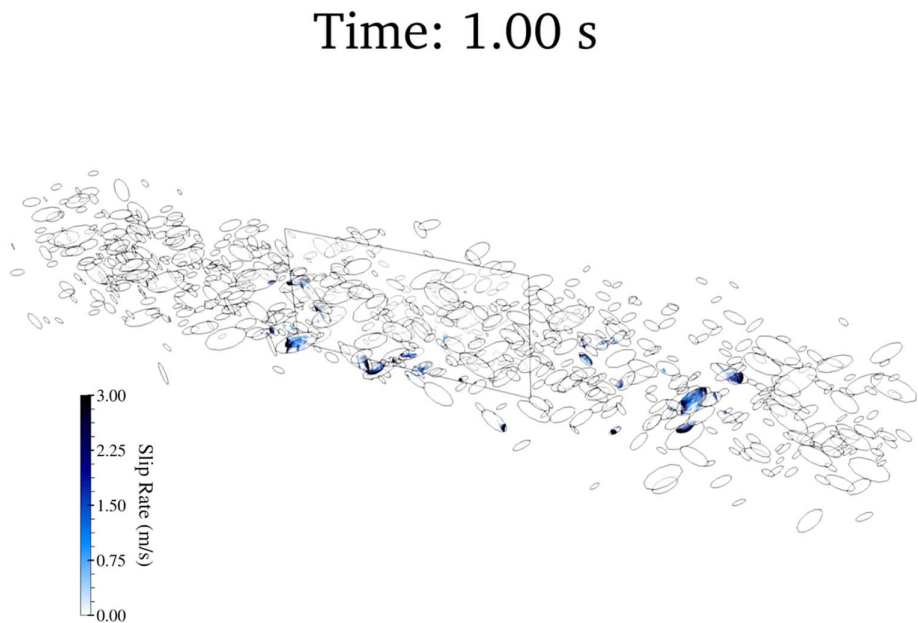
In the first case, fractures were predominantly unfavorably prestressed, leading to dynamic rupture primarily breaking the main fault and inducing off-fault fracture slip, which resembled asymmetric deformation patterns in nature and theoretical models (8, 65–67) (Fig. 3A). Fractures were unfavorably prestressed ($\mathcal{R} < 0.3$), yet 328 out of 721 fractures slipped predominantly at the respective dilatational sides of the main fault (Movie 1; fig. S12, A and D to F; and movie S1).

By contrast, the second case, with both the fracture network and the main fault more optimally oriented, facilitated a sustained rupture cascade, branching and jumping across 482 discrete fractures without triggering sustained slip on the main fault (Fig. 3B, Movie 2, and movie S2). The cascade took the form of a dynamic rupture pulse (38), with a band of fractures actively slipping at any point in time. This multifault dynamic rupture was sustained entirely within a 3D fracture network, generating a sizable earthquake cascade without activating a main fault. In this case, the fractures and the main fault were more optimally prestressed ($0.6 < \mathcal{R} \leq 0.8$) owing to a different orientation of S_{Hmax} , whereas all other model parameters remained the same as in the first case. Slip across the fracture network was determined by intricate interactions of zigzagging rupture fronts and variations in static and dynamic stresses. Coulomb-stress changes due to the evolving slip in the fracture network and dynamic shear and normal stresses transported by seismic waves were jointly driving the dynamic rupture cascade. The far-field source mechanism was strike-slip but was misaligned with the main fault orientation. The band of actively slipping fractures had a similar apparent pulse width as the largest fracture in the network (≈ 500 m). The cascade rise time, the duration of slip at a given hypocentral distance within the fault zone, was short compared with the overall rupture duration of the cascade ($\sim 10\%$) at all azimuths (fig. S12, B, D, E, and G).

In the third case, with closer-to-critical prestress conditions on the fractures and the main fault, the earthquake cascade dynamically triggered the main fault after 2.1 s, resulting in a



Movie 1. Evolution of absolute slip rate (meters per second) for the dynamic rupture simulation case 1 (Fig. 3A) in exploded view.



Movie 2. Evolution of absolute slip rate (meters per second) for the dynamic rupture simulation case 2 (Fig. 3B) in exploded view.

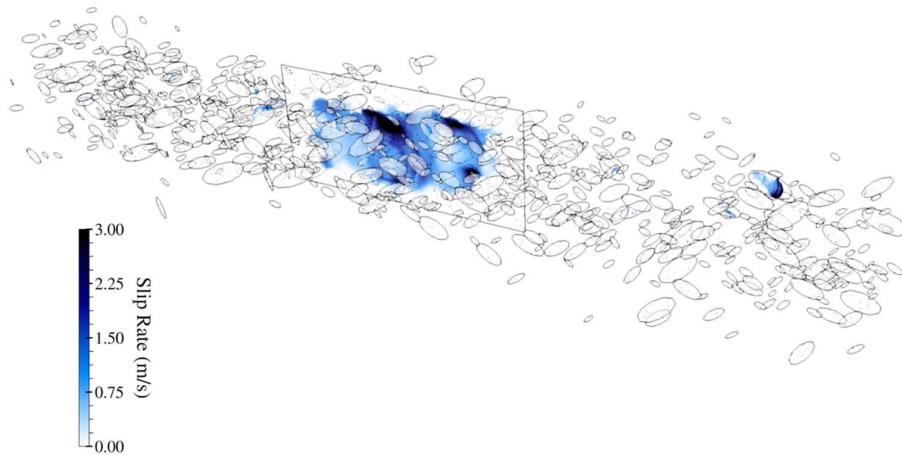
compound event with delayed main fault rupture (Fig. 3C, Movie 3, and movie S3). Fractures and the main fault were critically prestressed ($0.8 < \mathcal{R} \leq 0.95$) owing to a larger magnitude of \mathcal{R} , whereas all other model parameters were the same as in the second case. The dynamic rupture cascade in the fault damage zone contributed 42% of the total seismic moment release (Fig. S12, C to E and H).

Cases 4 to 14 explore the effects of scale-dependent or constant small and large fracture energy, varying prestress conditions, and frictional parameters on the cascading rup-

ture dynamics, as well as a comparison to weakening because of thermal pressurization (figs. S8 to S10 and S13 to S14 and movies S4 to S14) (51). For example, the fourth case (fig. S8A) demonstrates the importance of assuming fault size-dependent fracture energy. Assuming uniformly large G_c values for all fractures and the main fault leads to main-fault slip but fails to activate smaller multifracture ruptures.

Despite the complexity of the multifault earthquake cascades in our 3D dynamic rupture simulations, the resulting dynamic evolution of G_c aligns with our proposed scaling

Time: 2.50 s



Movie 3. Evolution of absolute slip rate (meters per second) for the dynamic rupture simulation case 3 (Fig. 3C) in exploded view.

with R (fig. S11). The consistency of our proposed linear scaling across two simplified analytical models and a range of complex dynamic simulations underscores the robustness of our proposed scaling mechanism.

The macroscopic kinematics of the dynamic rupture cascades (fig. S12) highlight distinct, potentially observable features: slow apparent cascading rupture speed ($\sim 0.65c_s$, with c_s being the S-wave speed) (fig. S12B) despite localized occurrences of supershear rupture speeds, short rise times (fig. S12C), multipeak moment rate release corresponding to multiple subevents of cascading fracture network slip (fig. S12D), and realistic high-frequency seismic radiation and realistic average stress drops, which are elevated for cascading dynamic ruptures (fig. S12, E to H).

Further analysis is required to better understand the interplay of our proposed scaling with additional types of stress heterogeneity, such as scale-dependent initial stress (18), or process-dependent dissipative processes, such as off-fault plasticity (68), in influencing rupture cascading and earthquake nucleation processes. During the modeled rupture cascades, coseismic stress transfer plays a crucial role, either reducing or augmenting local stresses of adjacent fault segments dynamically and statically. Capturing other forms of stress heterogeneity, such as those emerging from earthquake sequences or aseismic slip, may necessitate 3D earthquake cycle simulations that incorporate spontaneous (aseismic) nucleation conjointly with dynamic rupture (69–71), which are, however, methodologically and computationally challenging

at the same level of geometric and frictional complexity (72).

Discussion and conclusions

Fracture energy, the average energy dissipated during an earthquake, is commonly inferred from seismological observations by using idealized rupture models. Thus, the implications of our fault size-dependent fracture energy model extend beyond theoretical analyses. Our models add to data-consistent and physics-grounded explanations for why the dynamics of earthquakes often involve the activation of interconnected multifault systems spanning a variety of spatial scales (e.g., the 1992 Landers, California; 2016 Kaikōura, New Zealand; and 2023 Kahramanmaraş, Türkiye, earthquakes). The 2019 Ridgecrest earthquake sequence is a case in point, rupturing a conjugate multiscale fault system (3) comprising northeastern and northwestern trending high-angle strike-slip faults. Our scaling supports the mechanical viability of composite earthquake ruptures occurring as cascades over networks of faults of diverse sizes. Our analytical models show that statically strong but dynamically weak faults may drive multifault rupture cascades. In addition, our 3D dynamic rupture cascade simulations highlight the importance of dynamic and static stress transfers between variably oriented fault segments.

Our model provides an intuitive explanation for earthquakes observed across all scales, including potential seismicity occurring entirely off of main faults, such as within subsidiary fracture networks within the damage zone. High-resolution optical satellite image corre-

lation has confirmed the importance of distributed faulting and diffuse deformation, accounting for up to 50% of coseismic surface displacement (73). This aligns with the off-fault versus main-fault slip partitioning in our model of a multifracture rupture cascade dynamically triggering a main fault (Fig. 3C and Movie 3). The diverse slip directions observed in off-fault fractures (Fig. 4A) may not be explained by background or static stress changes alone (74) and resemble the variability of rake directions in our dynamic fracture network cascades (Fig. 4, B and C). Our hypothesis may also shed light on the intriguing observation that far-field focal mechanisms of large earthquakes can be misaligned with their main fault plane (75) as well as with the focal mechanisms of “volumetric” aftershocks (76). Such misalignments may be attributed to cascading fault zone ruptures driven by fault size-dependent fracture energy. Even on smaller scales, such as during the 2016 to 2019 Cahuilla earthquake swarm (77), volumetric seismicity is complex, potentially indicating multifracture network rupture phenomena. Some previous explanations for the scaling of observed fracture energy fail to account for small earthquakes because faults smaller than the nucleation size R_c are theoretically unable to nucleate dynamic rupture. For example, we derive that $R_c \sim 31$ m for the continuous coseismic weakening model under thermal pressurization (red line, Fig. 2B) (22, 51). Assuming a plausible stress drop of 10 MPa and homogeneous parameters, the thermal pressurization model fails to explain the seismogenesis of earthquakes smaller than $M_w \approx 2$.

Our findings have implications for the mechanics of natural fault systems and the earthquake cycle. We suggest that the redistribution of stresses by cascading ruptures in off-fault fracture networks may assist or inhibit the nucleation of larger events and account for dynamic variations in fault strength and stress, even when the main fault is weak, such as in subduction zones (78). A cascading multifracture earthquake rupture initiation model (Fig. 4D) may include cascading compound off-fault seismicity driven by fault size-dependent minimum fracture energy G_c within a fracture or fault network leading to the nucleation of a large earthquake. This mechanism shares similarities with the classical “cascade” nucleation model (27). However, in distinction to established earthquake nucleation models (79), our volumetric dynamic rupture cascades are dynamically driven and may initiate earthquakes with or without sustained rupture of a main fault.

The physical mechanisms behind our proposed simple linear scaling of the “small-slip” fracture energy with fault size present an intriguing topic for further investigation. Fault cores of large faults are embedded in fault

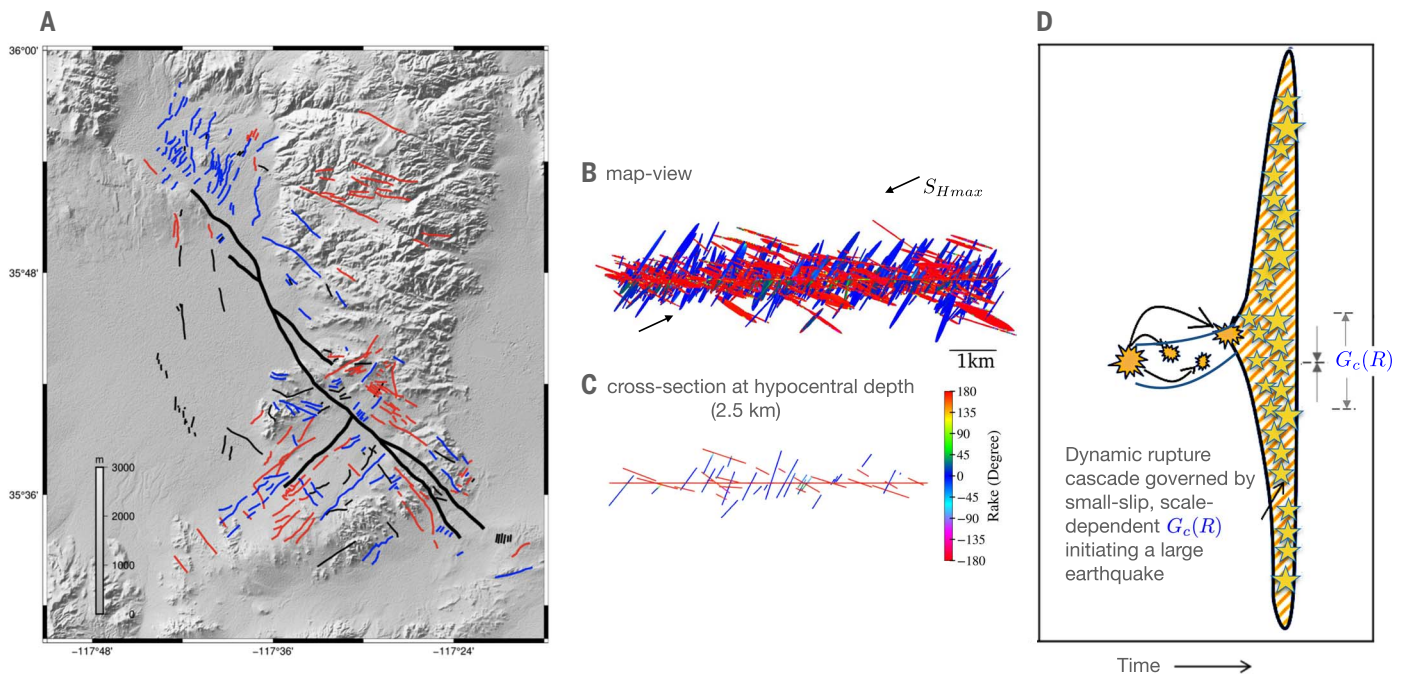


Fig. 4. Rupture maps and model output. (A) Map of coseismically activated off-fault fractures based on interferometric synthetic aperture radar (InSAR) data for the 2019 Ridgecrest earthquake sequence [adapted from (74)]. Black lines denote the main rupture trace and surface fractures that are not predominantly strike-slip. Red lines mark right lateral, and blue lines mark left lateral strike-slip motion. (B) Map view showing the variable rake across the complete fracture network in our 3D dynamic

rupture model after the rupture cascade dynamically triggers a main fault (Fig. 3C). (C) A horizontal cross section of (B) at a depth of 2.5 km to align with surface observations in (A). (D) Illustration of a multifault cascade earthquake initiation model modified from (27). Nucleation of a large earthquake by an off-fault dynamic rupture cascade within a fracture network driven by fault size-dependent minimum fracture energy G_c .

Downloaded from https://www.science.org at Universitaet Muenchen on July 26, 2024

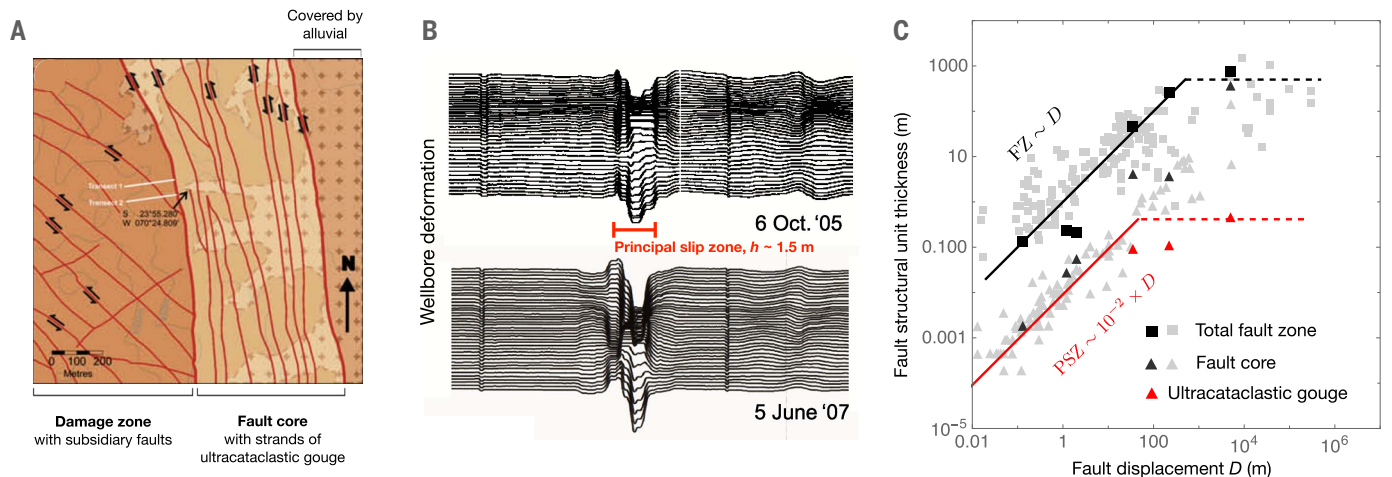


Fig. 5. Fault zones. (A) Geological map of the Caleta Coloso fault, showing a ≈ 400 -m-thick fault core with ≈ 1 -m-thick ultracataclastic gouge strands and a ≈ 200 -m-thick fault damage zone abating the fault core and hosting subsidiary faults and fractures [adapted from (8)]. (B) The ultracataclastic gouge zone of the San Andreas Fault intersected by the San Andreas Fault Observatory at Depth (SAFOD) wellbore, a principal slip zone with evidence of interseismically delocalized slip [adapted from (92)]. Black

lines represent the radial deformation of the wellbore casing at various azimuthal directions along its circumference. (C) Approximately linear scaling of the thicknesses of the total fault zone (FZ) and principal slip zone (PSZ) with total fault displacement D . We show the thicknesses of FZ (black squares) and PSZ (FC, black triangles; ultracataclastic gouge, red triangles) for six faults of varying size from (8) as well as a larger compilation of FZ (gray squares) from (9) and FC (gray triangles) from (93, 94).

damage zones that include subsidiary faults, enclosed lenses of highly fractured material, and distributed macrofractures (Fig. 5A). Within the fault core, strain is accommodated within one or several principal slip zones of highly constricted, ultracataclastic gouge of centimeter-

to-meter thickness and may coseismically localize to a submillimeter “slip surface” (9, 10, 80, 81). For example, deformation across the San Andreas Fault is distributed over the entire intersected gouge layer thickness of ≈ 1.5 m (Fig. 5B). This structural complexity is reduced for smaller

faults where a single fault core is embedded in a thin fault damage zone (8, 9). We compiled observations that suggest that the thickness of fault zones (FZs) and principal slip zones (PSZs) both scale approximately linearly with total fault displacement D as $FZ \sim D$ and

PSZ $\sim 10^{-2}D$ (Fig. 5C). The PSZ is here defined as an ultracataclastic gouge layer within the fault core (FC) of large faults or as the entire fault core for smaller, more immature faults. Both scaling relations saturate when faults exceed $D \approx 100$ m (PSZ) and $D \approx 300$ m (FZ). The empirical scaling relation $D \sim 10^{-2}L_f$ (7), where L_f is the fault length, suggests equivalent scaling relationships as FZ $\sim 10^{-2}L_f$ and PSZ $\sim 10^{-4}L_f$.

Localization of brittle deformation before and during earthquakes is highlighted in laboratory experiments, theoretical models, and statistical analyses of seismicity (20, 82–86). In the context of localization, the “small-slip” minimum fracture energy G_c may be interpreted as the fracture energy of a coseismic localization process. In this case, we expect that G_c scales with the thickness of the fault’s principal slip zone (Fig. 5), which itself scales with total fault displacement and fault length. Thereby, localization offers a physical mechanism explaining the onset of flash-heating weakening related to the dramatic colocalization drop of fault strength informing G_c . Subsequent postlocalization slip may favor more efficient pore fluid thermal pressurization (20, 22), leading to continuing weakening with slip (Fig. 2B) in the “tail” of the earthquake rupture (87). Thus, this process can also explain the emergence of the second, “large-slip” term $\Delta G(\delta)$ in our fracture energy decomposition (Eq. 4) that is not confined to the rupture “tip” or “body.”

Our fault size-dependent fracture energy model offers an intuitive and comprehensive framework for understanding the complexity of earthquakes across different scales. By acknowledging that distinct “small-slip” and “large-slip” fracture energy components govern earthquake dynamics, we provide new insights into the mechanisms driving earthquake nucleation, propagation, and cascading in natural fault zones. In an era in which seismology is increasingly “data rich,” the community often remains “model poor,” marked by a scarcity of mechanically consistent theoretical frameworks for understanding earthquake mechanics across scales. Our model is a crucial step toward bridging this gap, enhancing theoretical capabilities for understanding and thus potentially forecasting earthquake dynamics.

Materials and methods summary

We derived an expression for $G^* = G - G'$ using an analytical model for circular cracklike dynamic rupture driven by flash-heating friction and accounting for coseismic fault restrengthening. We considered a 3D cracklike circular dynamic rupture on a fault with rate- and state-dependent, flash-heating friction (20, 41). Next, we derived an analytical model for a bilaterally expanding kinematic pulse-like rupture based on general stress recovery princi-

ples in the wake of slip pulses. Both models establish a quasilinear scaling of dynamic undershoot with rupture size, which is a central aspect of our linear scaling of G^* with ruptured fault size. We compiled fracture energy and related earthquake source quantities, such as average slip and ruptured fault size, for five different data sets: (i) small earthquakes, (ii) large crustal earthquakes, (iii) large subduction zone earthquakes, (iv) 3D dynamic rupture models of well-recorded earthquakes, and (v) 3D dynamic and quasidynamic models of repeating earthquakes. We discuss challenges in estimating these earthquake source parameters. We used 3D dynamic rupture simulations and scale-dependent fracture energy to demonstrate the dynamic interactions of coseismic, cascading slip across a major fault interacting with a fracture network in its damage zone. We used supercomputing to apply our proposed scaling and unveil large earthquake cascades involving more than 700 multiscale fractures within a fault damage zone capable of dynamically triggering a main fault. We show a total of 14 3D dynamic rupture simulations across the same fault-fracture network system geometry. For details, see the supplementary materials (51).

REFERENCES AND NOTES

- Z. Jia *et al.*, The complex dynamics of the 2023 Kahramanmaraş, Turkey, M_w 7.8–7.7 earthquake doublet. *Science* **381**, 985–990 (2023). doi: [10.1126/science.adf0685](https://doi.org/10.1126/science.adf0685); pmid: [37535759](https://pubmed.ncbi.nlm.nih.gov/37535759/)
- P. M. Mai *et al.*, The Destructive Earthquake Doublet of 6 February 2023 in South-Central Türkiye and Northwestern Syria: Initial Observations and Analyses. *The Seismic Record* **3**, 105–115 (2023). doi: [10.1785/0320230007](https://doi.org/10.1785/0320230007)
- Z. E. Ross *et al.*, Hierarchical interlocked orthogonal faulting in the 2019 Ridgecrest earthquake sequence. *Science* **366**, 346–351 (2019). doi: [10.1126/science.aaz0109](https://doi.org/10.1126/science.aaz0109); pmid: [31624209](https://pubmed.ncbi.nlm.nih.gov/31624209/)
- K. Aki, Scaling law of seismic spectrum. *J. Geophys. Res.* **72**, 1217 (1967).
- R. E. Abercrombie, Earthquake source scaling relationships from -1 to $5 M_L$ using seismograms recorded at 2.5-km depth. *J. Geophys. Res.* **100**, 24015–24036 (1995). doi: [10.1029/95JB02397](https://doi.org/10.1029/95JB02397)
- S. Ide, G. C. Beroza, Does apparent stress vary with earthquake size? *Geophys. Res. Lett.* **28**, 3349–3352 (2001). doi: [10.1029/2001GL013106](https://doi.org/10.1029/2001GL013106)
- C. H. Scholz, *The mechanics of earthquakes and faulting* (Cambridge University Press, 2019). doi: [10.1017/9781316681473](https://doi.org/10.1017/9781316681473)
- T. Mitchell, D. Faulkner, The nature and origin of off-fault damage surrounding strike-slip fault zones with a wide range of displacements: A field study from the Atacama fault system, northern Chile. *J. Struct. Geol.* **31**, 802–816 (2009). doi: [10.1016/j.jsg.2009.05.002](https://doi.org/10.1016/j.jsg.2009.05.002)
- H. M. Savage, E. E. Brodsky, Collateral damage: Evolution with displacement of fracture distribution and secondary fault strands in fault damage zones. *J. Geophys. Res. Solid Earth* **116**, B03405 (2011). doi: [10.1029/2010JB007665](https://doi.org/10.1029/2010JB007665)
- F. M. Chester, J. P. Evans, R. L. Biegel, Internal structure and weakening mechanisms of the San Andreas Fault. *J. Geophys. Res.* **98**, 771–786 (1993). doi: [10.1029/92JB01866](https://doi.org/10.1029/92JB01866)
- M. Cocco *et al.*, Fracture Energy and Breakdown Work During Earthquakes. *Annu. Rev. Earth Planet. Sci.* **51**, 217–252 (2023). doi: [10.1146/annurev-earth-071822-100304](https://doi.org/10.1146/annurev-earth-071822-100304)
- R. E. Abercrombie, Resolution and uncertainties in estimates of earthquake stress drop and energy release. *Philos. Trans. A Math. Phys. Eng. Sci.* **379**, 20200131 (2021). doi: [10.1098/rsta.2020.0131](https://doi.org/10.1098/rsta.2020.0131); pmid: [33715406](https://pubmed.ncbi.nlm.nih.gov/33715406/)
- G. Kwiatek, K. Plenkens, M. Nakatani, Y. Yabe, G. Dresen, Frequency-Magnitude Characteristics Down to Magnitude -4.4 for Induced Seismicity Recorded at Mponeng Gold Mine, South

- Africa. *Bull. Seismol. Soc. Am.* **100**, 1165–1173 (2010). doi: [10.1785/0120090277](https://doi.org/10.1785/0120090277)
- J. R. Rice, *Physics of the Earth's Interior, course 78* of Proceedings of the International School of Physics “Enrico Fermi,” A. Dziewonski, E. Boschi, Eds. (IOS Press, 1980), pp. 555–649.
- L. B. Freund, *Dynamic Fracture Mechanics* (Cambridge Univ. Press, 1998).
- G. Di Toro *et al.*, Fault lubrication during earthquakes. *Nature* **471**, 494–498 (2011). doi: [10.1038/nature09838](https://doi.org/10.1038/nature09838); pmid: [21430777](https://pubmed.ncbi.nlm.nih.gov/21430777/)
- F. Paglialunga *et al.*, On the scale dependence in the dynamics of frictional rupture: Constant fracture energy versus size-dependent breakdown work. *Earth Planet. Sci. Lett.* **584**, 117442 (2022). doi: [10.1016/j.epsl.2022.117442](https://doi.org/10.1016/j.epsl.2022.117442)
- C.-Y. Ke, G. C. McLaskey, D. S. Kammer, Earthquake breakdown energy scaling despite constant fracture energy. *Nat. Commun.* **13**, 1005 (2022). doi: [10.1038/s41467-022-28647-4](https://doi.org/10.1038/s41467-022-28647-4); pmid: [35194043](https://pubmed.ncbi.nlm.nih.gov/35194043/)
- S. Ide, H. Aochi, Earthquakes as multiscale dynamic ruptures with heterogeneous fracture surface energy. *J. Geophys. Res. Solid Earth* **110**, B11303 (2005).
- J. R. Rice, Heating and weakening of faults during earthquake slip. *J. Geophys. Res. Solid Earth* **111**, B05311 (2006).
- M. Cocco, E. Tinti, C. Marone, A. Piatanesi, Scaling of Slip Weakening Distance with Final Slip during Dynamic Earthquake Rupture. *International Geophysics* **94**, 163–186 (2009). doi: [10.1016/S0074-6142\(08\)00007-7](https://doi.org/10.1016/S0074-6142(08)00007-7)
- R. C. Viesca, D. I. Garagash, Ubiquitous weakening of faults due to thermal pressurization. *Nat. Geosci.* **8**, 875–879 (2015). doi: [10.1038/ngeo2554](https://doi.org/10.1038/ngeo2554)
- P. M. Mai *et al.*, On Scaling of Fracture Energy and Stress Drop in Dynamic Rupture Models: Consequences for Near-Source Ground-Motion. *Geophys. Monogr.* **170**, 283 (2006).
- Y. Ben-Zion, G. C. Beroza, M. Bohnhoff, A. Gabriel, P. M. Mai, A Grand Challenge International Infrastructure for Earthquake Science. *Seismol. Res. Lett.* **93**, 2967–2968 (2022). doi: [10.1785/0220220266](https://doi.org/10.1785/0220220266)
- A. Udías, R. Madariaga, E. Buforn, *Source mechanisms of earthquakes: Theory and practice* (Cambridge Univ. Press, 2014).
- T. Mikumo, K. B. Olsen, E. Fukuyama, Y. Yagi, Stress-Breakdown Time and Slip-Weakening Distance Inferred from Slip-Velocity Functions on Earthquake Faults. *Bull. Seismol. Soc. Am.* **93**, 264–282 (2003). doi: [10.1785/0120020082](https://doi.org/10.1785/0120020082)
- G. C. McLaskey, Earthquake Initiation From Laboratory Observations and Implications for Foreshocks. *J. Geophys. Res. Solid Earth* **124**, 12882–12904 (2019). doi: [10.1029/2019JB018363](https://doi.org/10.1029/2019JB018363)
- B. V. Kostrov, S. Das, *Principles of earthquake source mechanics* (Cambridge Univ. Press, 1988).
- R. E. Abercrombie, J. R. Rice, Can observations of earthquake scaling constrain slip weakening? *Geophys. J. Int.* **162**, 406–424 (2005). doi: [10.1111/j.1365-246X.2005.02579.x](https://doi.org/10.1111/j.1365-246X.2005.02579.x)
- V. Lambert, N. Lapusta, S. Perry, Propagation of large earthquakes as self-healing pulses or mild cracks. *Nature* **591**, 252–258 (2021). doi: [10.1038/s41586-021-03248-1](https://doi.org/10.1038/s41586-021-03248-1); pmid: [33692555](https://pubmed.ncbi.nlm.nih.gov/33692555/)
- H. Kanamori, T. H. Heaton, Microscopic and macroscopic physics of earthquakes. *Geophys. Monogr.* **120**, 147–163 (2000). doi: [10.1029/GM120p0147](https://doi.org/10.1029/GM120p0147)
- E. Tinti, P. Spudich, M. Cocco, Earthquake fracture energy inferred from kinematic rupture models on extended faults. *J. Geophys. Res. Solid Earth* **110**, B12303 (2005).
- H. Noda, N. Lapusta, H. Kanamori, Comparison of average stress drop measures for ruptures with heterogeneous stress change and implications for earthquake physics. *Geophys. J. Int.* **193**, 1691–1712 (2013). doi: [10.1093/gji/ggt074](https://doi.org/10.1093/gji/ggt074)
- M. Ohnaka *et al.*, A constitutive law for the shear failure of rock under lithospheric conditions. *Tectonophysics* **277**, 1–27 (1997). doi: [10.1016/S0040-1951\(97\)00075-9](https://doi.org/10.1016/S0040-1951(97)00075-9)
- N. Brantut, R. C. Viesca, Earthquake nucleation in intact or healed rocks. *J. Geophys. Res. Solid Earth* **120**, 191–209 (2015). doi: [10.1002/2014JB011518](https://doi.org/10.1002/2014JB011518)
- R. Madariaga, Dynamics of an expanding circular fault. *Bull. Seismol. Soc. Am.* **66**, 639–666 (1976). doi: [10.1785/BSSA0660030639](https://doi.org/10.1785/BSSA0660030639)
- F. Galloway, L. Valentova, J.-P. Ampuero, A.-A. Gabriel, Bayesian Dynamic Finite-Fault Inversion: 2. Application to the 2016 M_w 6.2 Amatrice, Italy, Earthquake. *J. Geophys. Res. Solid Earth* **124**, 6970–6988 (2019). doi: [10.1029/2019JB017512](https://doi.org/10.1029/2019JB017512)
- T. H. Heaton, Evidence for and implications of self-healing pulses of slip in earthquake rupture. *Phys. Earth Planet. Inter.* **64**, 1–20 (1990). doi: [10.1016/0031-9201\(90\)90002-F](https://doi.org/10.1016/0031-9201(90)90002-F)

39. M. Causse, L. Dalguer, P. Mai, Variability of dynamic source parameters inferred from kinematic models of past earthquakes. *Geophys. J. Int.* **196**, 1754–1769 (2014). doi: [10.1093/gji/ggt478](https://doi.org/10.1093/gji/ggt478)
40. N. Brantut, R. C. Viesca, The fracture energy of ruptures driven by flash heating. *Geophys. Res. Lett.* **44**, 6718–6725 (2017). doi: [10.1002/2017GL074110](https://doi.org/10.1002/2017GL074110)
41. H. Noda, E. M. Dunham, J. R. Rice, Earthquake ruptures with thermal weakening and the operation of major faults at low overall stress levels. *J. Geophys. Res. Solid Earth* **114**, B07302 (2009).
42. J. D. Platt, R. C. Viesca, D. I. Garagash, Steadily propagating slip pulses driven by thermal decomposition. *J. Geophys. Res. Solid Earth* **120**, B012200 (2015). doi: [10.1002/2015JB012200](https://doi.org/10.1002/2015JB012200)
43. A.-A. Gabriel, J.-P. Ampuero, L. A. Dalguer, P. M. Mai, The transition of dynamic rupture styles in elastic media under velocity-weakening friction. *J. Geophys. Res. Solid Earth* **117**, B09311 (2012).
44. G. Zheng, J. R. Rice, Conditions under which velocity-weakening friction allows a self-healing versus a cracklike mode of rupture. *Bull. Seismol. Soc. Am.* **88**, 1466–1483 (1998). doi: [10.1785/BSSA0880061466](https://doi.org/10.1785/BSSA0880061466)
45. D. I. Garagash, Seismic and aseismic slip pulses driven by thermal pressurization of pore fluid. *J. Geophys. Res. Solid Earth* **117**, B04314 (2012).
46. N. Brantut, D. I. Garagash, H. Noda, Stability of Pulse-Like Earthquake Ruptures. *J. Geophys. Res. Solid Earth* **124**, 8998–9020 (2019). doi: [10.1029/2019JB017926](https://doi.org/10.1029/2019JB017926)
47. D. L. Goldsby, T. E. Tullis, Flash heating leads to low frictional strength of crustal rocks at earthquake slip rates. *Science* **334**, 216–218 (2011). doi: [10.1126/science.1207902](https://doi.org/10.1126/science.1207902); pmid: [21998385](https://pubmed.ncbi.nlm.nih.gov/21998385/)
48. A. H. Kohli, D. L. Goldsby, G. Hirth, T. Tullis, Flash weakening of serpentinite at near-seismic slip rates. *J. Geophys. Res. Solid Earth* **116**, B03202 (2011).
49. F. Barras *et al.*, The emergence of crack-like behavior of frictional rupture: Edge singularity and energy balance. *Earth Planet. Sci. Lett.* **531**, 115978 (2020). doi: [10.1016/j.epsl.2019.115978](https://doi.org/10.1016/j.epsl.2019.115978)
50. D. I. Garagash, Fracture mechanics of rate-and-state faults and fluid injection induced slip. *Philos. Trans. A Math. Phys. Eng. Sci.* **379**, 20200129 (2021). doi: [10.1098/rsta.2020.0129](https://doi.org/10.1098/rsta.2020.0129); pmid: [33715418](https://pubmed.ncbi.nlm.nih.gov/33715418/)
51. Materials and methods are available as supplementary materials.
52. B. Kostrov, Self-similar problems of propagation of shear cracks. *J. Appl. Math. Mech.* **28**, 1077–1087 (1964). doi: [10.1016/0021-8928\(64\)90010-3](https://doi.org/10.1016/0021-8928(64)90010-3)
53. J. N. Brune, Tectonic stress and the spectra of seismic shear waves from earthquakes. *J. Geophys. Res.* **75**, 4997–5009 (1970). doi: [10.1029/JB075i026p04997](https://doi.org/10.1029/JB075i026p04997)
54. T. Taufiqurrahman *et al.*, Dynamics, interactions and delays of the 2019 Ridgecrest rupture sequence. *Nature* **618**, 308–315 (2023). doi: [10.1038/s41586-023-05985-x](https://doi.org/10.1038/s41586-023-05985-x); pmid: [3725989](https://pubmed.ncbi.nlm.nih.gov/3725989/)
55. K. H. Palgunadi, A.-A. Gabriel, T. Ulrich, J. Á. López-Comino, P. M. Mai, Dynamic Fault Interaction during a Fluid-Injection-Induced Earthquake: The 2017 Mw 5.5 Pohang Event. *Bull. Seismol. Soc. Am.* **110**, 2328–2349 (2020). doi: [10.1785/0120200106](https://doi.org/10.1785/0120200106)
56. T. Taufiqurrahman, A.-A. Gabriel, T. Ulrich, L. Valentova, F. Gallovič, Broadband Dynamic Rupture Modeling With Fractal Fault Roughness, Frictional Heterogeneity, Viscoelasticity and Topography: The 2016 Mw 6.2 Amatrice, Italy Earthquake. *Geophys. Res. Lett.* **49**, e2022GL098872 (2022). doi: [10.1029/2022GL098872](https://doi.org/10.1029/2022GL098872)
57. T. Ulrich *et al.*, Coupled, Physics-Based Modeling Reveals Earthquake Displacements are Critical to the 2018 Palu, Sulawesi Tsunami. *Pure Appl. Geophys.* **176**, 4069–4109 (2019). doi: [10.1007/s00024-019-02290-5](https://doi.org/10.1007/s00024-019-02290-5)
58. S. Wollherr, A.-A. Gabriel, P. M. Mai, Landers 1992 “Reloaded”: Integrative Dynamic Earthquake Rupture Modeling. *J. Geophys. Res. Solid Earth* **124**, 6666–6702 (2019). doi: [10.1029/2018JB016355](https://doi.org/10.1029/2018JB016355)
59. T. Ulrich, A.-A. Gabriel, J.-P. Ampuero, W. Xu, Dynamic viability of the 2016 Mw 7.8 Kaikōura earthquake cascade on weak crustal faults. *Nat. Commun.* **10**, 1213 (2019). doi: [10.1038/s41467-019-09125-w](https://doi.org/10.1038/s41467-019-09125-w); pmid: [30872591](https://pubmed.ncbi.nlm.nih.gov/30872591/)
60. T. Ulrich, A.-A. Gabriel, E. H. Madden, Stress, rigidity and sediment strength control megathrust earthquake and tsunami dynamics. *Nat. Geosci.* **15**, 67–73 (2022). doi: [10.1038/s41561-021-00863-5](https://doi.org/10.1038/s41561-021-00863-5)
61. S. K. Y. Lui, N. Lapusta, Modeling High Stress Drops, Scaling, Interaction, and Irregularity of Repeating Earthquake Sequences Near Parkfield. *J. Geophys. Res. Solid Earth* **123**, 10,854 (2018). doi: [10.1029/2018JB016472](https://doi.org/10.1029/2018JB016472)
62. K. Ariyoshi *et al.*, A trial estimation of frictional properties, focusing on aperiodicity off Kamaishi just after the 2011 Tohoku earthquake. *Geophys. Res. Lett.* **41**, 8325–8334 (2014). doi: [10.1002/2014GL061872](https://doi.org/10.1002/2014GL061872)
63. N. Uchida, K. Shimamura, T. Matsuzawa, T. Okada, Postseismic response of repeating earthquakes around the 2011 Tohoku-oki earthquake: Moment increases due to the fast loading rate. *J. Geophys. Res. Solid Earth* **120**, 259–274 (2015). doi: [10.1002/2013JB010933](https://doi.org/10.1002/2013JB010933)
64. K. H. Palgunadi, A.-A. Gabriel, D. I. Garagash, T. Ulrich, P. M. Mai, Rupture Dynamics of Cascading Earthquakes in a Multiscale Fracture Network. *J. Geophys. Res. Solid Earth* **129**, e2023JB027578 (2024). doi: [10.1029/2023JB027578](https://doi.org/10.1029/2023JB027578)
65. D. Andrews, Rupture dynamics with energy loss outside the slip zone. *J. Geophys. Res. Solid Earth* **110**, B01307 (2005).
66. C. Perrin, I. Manighetti, J.-P. Ampuero, F. Cappa, Y. Gaudemer, Location of largest earthquake slip and fast rupture controlled by along-strike change in fault structural maturity due to fault growth. *J. Geophys. Res. Solid Earth* **121**, 3666–3685 (2016). doi: [10.1002/2015JB012671](https://doi.org/10.1002/2015JB012671)
67. K. Okubo *et al.*, Dynamics, Radiation, and Overall Energy Budget of Earthquake Rupture With Coseismic Off-Fault Damage. *J. Geophys. Res. Solid Earth* **124**, 11771–11801 (2019). doi: [10.1029/2019JB017304](https://doi.org/10.1029/2019JB017304)
68. M. S. Mia, M. Abdelmeguid, R. A. Harris, A. E. Elbanna, Rupture Jumping and Seismic Complexity in Models of Earthquake Cycles for Fault Steepeners with Off-Fault Plasticity. *Bull. Seismol. Soc. Am.* **114**, 1466–1480 (2024). doi: [10.1785/0120230249](https://doi.org/10.1785/0120230249)
69. N. Lapusta, Y. Liu, Three-dimensional boundary integral modeling of spontaneous earthquake sequences and aseismic slip. *J. Geophys. Res. Solid Earth* **114**, B09303 (2009).
70. B. Luo, B. Duan, D. Liu, 3D Finite-Element Modeling of Dynamic Rupture and Aseismic Slip over Earthquake Cycles on Geometrically Complex Faults. *Bull. Seismol. Soc. Am.* **110**, 2619–2637 (2020). doi: [10.1785/0120200047](https://doi.org/10.1785/0120200047)
71. J. Jiang *et al.*, Community-Driven Code Comparisons for Three-Dimensional Dynamic Modeling of Sequences of Earthquakes and Aseismic Slip. *J. Geophys. Res. Solid Earth* **127**, e2021JB023519 (2022).
72. C. Uphoff, D. A. May, A.-A. Gabriel, A discontinuous Galerkin method for sequences of earthquakes and aseismic slip on multiple faults using unstructured curvilinear grids. *Geophys. J. Int.* **233**, 586–626 (2023). doi: [10.1093/gji/ggac467](https://doi.org/10.1093/gji/ggac467)
73. S. L. Antoine *et al.*, Diffuse Deformation and Surface Faulting Distribution from Submetric Image Correlation along the 2019 Ridgecrest, California, Ruptures. *Bull. Seismol. Soc. Am.* **111**, 2275–2302 (2021). doi: [10.1785/0120210036](https://doi.org/10.1785/0120210036)
74. X. Xu, D. T. Sandwell, B. Smith-Konter, Coseismic Displacements and Surface Fractures from Sentinel-1 InSAR: 2019 Ridgecrest Earthquakes. *Seismol. Res. Lett.* **91**, 1979–1985 (2020). doi: [10.1785/0220190275](https://doi.org/10.1785/0220190275)
75. D. R. Scott, H. Kanamori, On the consistency of moment tensor source mechanisms with first-motion data. *Phys. Earth Planet. Inter.* **37**, 97–107 (1985). doi: [10.1016/0031-9201\(85\)90044-5](https://doi.org/10.1016/0031-9201(85)90044-5)
76. E. Hauksson, L. M. Jones, K. Hutton, The 1999 Mw 7.1 Hector Mine, California, Earthquake Sequence: Complex Conjugate Strike-Slip Faulting. *Bull. Seismol. Soc. Am.* **92**, 1154–1170 (2002). doi: [10.1785/0120000920](https://doi.org/10.1785/0120000920)
77. E. S. Cochran, M. T. Page, N. J. van der Elst, Z. E. Ross, D. T. Trugman, Fault Roughness at Seismogenic Depths and Links to Earthquake Behavior. *The Seismic Record* **3**, 37–47 (2023). doi: [10.1785/0320220043](https://doi.org/10.1785/0320220043)
78. S. Shreedharan, D. Saffer, L. M. Wallace, C. Williams, Ultralow frictional healing explains recurring slow slip events. *Science* **379**, 712–717 (2023). doi: [10.1126/science.adf4930](https://doi.org/10.1126/science.adf4930); pmid: [36795827](https://pubmed.ncbi.nlm.nih.gov/36795827/)
79. P. Martínez-Garzón, Poli, *Commun. Earth Environ.* **5**, 120 (2024). doi: [10.1038/s43247-024-01285-y](https://doi.org/10.1038/s43247-024-01285-y)
80. F. M. Chester, J. S. Chester, Ultracataclastic structure and friction processes of the Punchbowl fault, San Andreas system, California. *Tectonophysics* **295**, 199–221 (1998). doi: [10.1016/S0040-1951\(98\)00121-8](https://doi.org/10.1016/S0040-1951(98)00121-8)
81. N. De Paola, C. Colletti, D. R. Faulkner, F. Trippetta, Fault zone architecture and deformation processes within evaporitic rocks in the upper crust. *Tectonics* **27**, 2007TC002230 (2008). doi: [10.1029/2007TC002230](https://doi.org/10.1029/2007TC002230)
82. D. Lockner, J. Byerlee, V. Kuksenko, A. Ponomarev, A. Sidorin, Quasi-static fault growth and shear fracture energy in granite. *Nature* **350**, 39–42 (1991). doi: [10.1038/350039a0](https://doi.org/10.1038/350039a0)
83. Y. Ben-Zion, I. Zaliapin, Localization and coalescence of seismicity before large earthquakes. *Geophys. J. Int.* **223**, 561–583 (2020). doi: [10.1093/gji/ggaa315](https://doi.org/10.1093/gji/ggaa315)
84. J. D. Platt, J. W. Rudnicki, J. R. Rice, Stability and localization of rapid shear in fluid-saturated fault gouge: 2. Localized zone width and strength evolution. *J. Geophys. Res. Solid Earth* **119**, 4334–4359 (2014). doi: [10.1002/2013JB010711](https://doi.org/10.1002/2013JB010711)
85. B. P. Proctor *et al.*, Dynamic weakening of serpentinite gouges and bare surfaces at seismic slip rates. *J. Geophys. Res. Solid Earth* **119**, 8107–8131 (2014). doi: [10.1002/2014JB011057](https://doi.org/10.1002/2014JB011057); pmid: [26167425](https://pubmed.ncbi.nlm.nih.gov/26167425/)
86. C. Pranger, P. Sanan, D. A. May, L. Le Pourhiet, A.-A. Gabriel, Rate and State Friction as a Spatially Regularized Transient Viscous Flow Law. *J. Geophys. Res. Solid Earth* **127**, e2021JB023511 (2022).
87. D. S. Kammer *et al.*, Energy dissipation in earthquakes. [arXiv:2403.06916](https://arxiv.org/abs/2403.06916) [physics.geo-ph] (2024).
88. M. Beyreuther *et al.*, ObsPy: A Python Toolbox for Seismology. *Seismol. Res. Lett.* **81**, 530–533 (2010). doi: [10.1785/gssrl.81.3.530](https://doi.org/10.1785/gssrl.81.3.530)
89. J. Ahrens, B. Geveci, C. Law, “Paraview: An End-User Tool for Large Data Visualization” in *The Visualization Handbook* (Elsevier, 2005), pp. 717–731.
90. J. D. Hunter, Matplotlib: A 2D Graphics Environment. *Comput. Sci. Eng.* **9**, 90–95 (2007). doi: [10.1109/MCSE.2007.55](https://doi.org/10.1109/MCSE.2007.55)
91. A.-A. Gabriel, D. Garagash, K. H. Palgunadi, P. M. Mai, SeisSol input files for “Fault-size dependent fracture energy explains multi-scale seismicity and cascading earthquakes,” Zenodo (2024); <https://doi.org/10.5281/zenodo.11208883>
92. M. Zoback, S. Hickman, W. Ellsworth, Scientific Drilling Into the San Andreas Fault Zone – An Overview of SAFOD’s First Five Years. *Sci. Drill.* **11**, 14–28 (2011). doi: [10.5194/sd-11-14-2011](https://doi.org/10.5194/sd-11-14-2011)
93. R. Marrett, R. W. Allmendinger, Kinematic analysis of fault-slip data. *J. Struct. Geol.* **12**, 973–986 (1990). doi: [10.1016/0191-8141\(90\)90093-E](https://doi.org/10.1016/0191-8141(90)90093-E)
94. E. C. Robertson, *ARMA US Rock Mechanics/Geomechanics Symposium* (ARMA, 1987), pp. ARMA–87.

ACKNOWLEDGMENTS

We thank T. Ulrich, N. Schliwa, and M. Marchandon for helping measure fracture energy in 3D dynamic rupture earthquake scenarios and R. Viesca for help with fig. S1 and helpful discussions. We thank H. Bhat, S. Marty, and F. Passelegue for helpful discussions. We thank all SeisSol developers (www.seissol.org), specifically S. Wolf, D. Schneller, and M. Bader. We thank the developers of the following open-source software packages that we used for data analysis and visualization: ObsPy (88), Paraview (89), and Matplotlib (90). **Funding:** Funding for this work was provided by the European Union’s Horizon 2020 Research and Innovation Programme (grant no. 852992 to A.-A.G.), Horizon Europe (grant nos. 101093038, 101058129, and 101058518 to A.-A.G.), the National Aeronautics and Space Administration (grant no. 80NSSC20K0495 to A.-A.G.), the National Science Foundation (grant nos. EAR-2121568, EAR-2225286, OAC-2139536, and OAC-2311208 to A.-A.G.), the Gauss Centre for Supercomputing (LRZ SuperMUC-NG project pn49ha to A.-A.G.), the Natural Sciences and Engineering Research Council of Canada (Discovery grant 05743 to D.I.G.) the Southern California Earthquake Center (SCEC awards 22135 and 23121 to A.-A.G.), KAUST research grants (BAS/1/1339-01-01 and URF/1/3389-01-01 to P.M.M.), and the Swiss Data Science Center (grant no. C22-10). **Author contributions:** Conceptualization: A.-A.G. and D.I.G.; Data curation: A.-A.G. and D.I.G.; Funding acquisition: A.-A.G., D.I.G., and P.M.M.; Formal analysis: A.-A.G., D.I.G., and K.H.P.; Methodology: A.-A.G., D.I.G., and K.H.P.; Project administration: A.-A.G. and P.M.M.; Resources: A.-A.G. and P.M.M.; Software: A.-A.G. and K.H.P.; Supervision: A.-A.G., D.I.G., and P.M.M.; Validation: A.-A.G. and D.I.G.; Visualization: A.-A.G., D.I.G., and K.H.P.; Writing – original draft: A.-A.G.; D.I.G., and K.H.P.; Writing – review and editing: A.-A.G., D.I.G., K.H.P., and P.M.M. **Competing interests:** The authors declare that they have no competing interests. **Data and materials availability:** The inferred fracture energy data presented in Fig. 2 and the corresponding references to the source parameters are available in supplementary information tables S.3 and S.4 of (22) for large subduction zone and crustal earthquakes, respectively, and from table S.5 for small crustal earthquakes. The new compilation of fault size-dependent fracture energy derived from data-constrained 3D

earthquake rupture scenarios of well-recorded real earthquakes is provided in our table S1. We use the commercial software FracMan Version 7.8 to generate the fracture network. The version of SeisSol used for the dynamic rupture models in Sec. 'Multi-fault earthquake cascades in 3D dynamic rupture simulations with fault-size-dependent fracture energy' is described in <https://seissol.readthedocs.io/en/latest/fault-tagging.html#using-more-than-189-dynamic-rupture-tags> with commit version 917250fd and from the branch SeisSol64FractureNetwork (<https://github.com/palgunadi1993/SeisSol/tree/SeisSol64FractureNetwork>). For the comparison to fault weakening due to thermal pressurization (case 14), we used SeisSol branch *fancy-lsw*. We used a patched version of the open-source meshing

software PUMGen, which can be cloned from the GitHub branch PUMGenFaceIdentification64bit (<https://github.com/palgunadi1993/PUMGen/tree/PUMGenFaceIdentification64bit>). Instructions for downloading, installing, and running SeisSol are available in SeisSol's online documentation at <https://seissol.readthedocs.io/>. Instructions for compiling SeisSol are available at <https://seissol.readthedocs.io/en/latest/compiling-seissol.html>. Instructions for setting up and running simulations are available at <https://seissol.readthedocs.io/en/latest/configuration.html>. All input and mesh files are available in the Zenodo repository (91). **License information:** Copyright © 2024 the authors, some rights reserved; exclusive licensee American Association for the Advancement of Science. No claim to original US government

works. <https://www.science.org/about/science-licenses-journal-article-reuse>

SUPPLEMENTARY MATERIALS

[science.org/doi/10.1126/science.adj9587](https://doi.org/10.1126/science.adj9587)

Materials and Methods

Figs. S1 to S14

Tables S1 to S4

References (95–148)

Movies S1 to S14

Submitted 28 July 2023; accepted 29 May 2024

10.1126/science.adj9587